

Ultraviolet Compactness of High-Redshift Galaxies as a Tracer of Early-Stage Gas Infall, Stochastic Star Formation, and Offset from the Fundamental Metallicity Relation

DANIAL LANGEROODI ¹ AND JENS HJORTH ¹

¹*DARK, Niels Bohr Institute, University of Copenhagen, Jagtvej 128, 2200 Copenhagen, Denmark*

ABSTRACT

The redshift evolution of the mass-metallicity relation is typically explained in terms of the fundamental metallicity relation (FMR), the empirical anti-correlation between the star-formation rate (SFR) and the gas-phase metallicity. At a fixed stellar mass, high-redshift galaxies have higher star-formation rates (SFR) and therefore lower gas-phase metallicities. Recent compilations of NIRSpect emission line galaxies have shown a mild redshift evolution of the FMR at $z > 4$, indicating that the FMR alone is not fully capable of capturing the redshift evolution of the mass-metallicity relation: $z > 4$ galaxies appear more metal-poor than the FMR predictions. There is evidence that the most metal-deficient high-redshift galaxies are also the most compact. In this work, we further investigate this anti-correlation by leveraging the wealth of data gathered through the first cycle of *JWST*. We compile a sample of 427 $z > 3$ galaxies covered by both the NIRSpect prism and NIRCAM short-wavelength photometry, consisting of 334 galaxies from the publicly available programs and 93 galaxies from the first data release of the JADES program. We use this sample to infer the redshift evolution of the FMR from $z = 3$ to $z \sim 10$, further confirming the previously reported mild redshift evolution. We measure the rest-ultraviolet (UV) sizes of $z > 4$ galaxies, inferring the mass-size relation at $z = 4 - 10$ with a power-law slope of 0.21 ± 0.04 . We investigate the redshift evolution of the mass-size relation, finding that at a fixed stellar mass, higher redshift galaxies appear more compact. The degree of this redshift evolution depends on the stellar mass, with the lowest mass galaxies showing the strongest redshift evolution and the most massive galaxies ($\log(M_*/M_\odot) > 9$) showing no redshift evolution. We investigate the anti-correlation between the compactness of galaxies and their gas-phase metallicities, finding that the more compact galaxies appear more metal-deficient and therefore more offset from the local calibration of the FMR. This suggests that the most compact high-redshift galaxies are undergoing their earliest stage of accretion on timescales much shorter than needed to achieve equilibrium between the infall, star formation, enrichment, and feedback-driven outflows. This supports the stochastic star-formation scenario for the simplest high redshift galaxies. Their compact sizes also support an inside-out star formation scenario, where the core of galaxies form early on during the centrally concentrated burst of star formation.

Keywords: High-redshift galaxies (734), Galaxy evolution (594), Galaxy chemical evolution (580), Chemical abundances (224), Metallicity (1031)

1. INTRODUCTION

The empirical correlation between the stellar mass and the gas-phase metallicity of galaxies (mass-metallicity relation) and the redshift evolution of this correlation have strong implications for our theories of galaxy for-

mation and evolution. The shape and normalization of this correlation are thought to be determined by the interplay between gas infall, star formation, chemical enrichment, and feedback-driven outflows. This makes the mass-metallicity relation and its redshift evolution some of the fundamental observables often reproduced by semi-analytic and numerical simulations (Schaye et al. 2015; Hirschmann et al. 2016; Lagos et al. 2016; Ma et al. 2016; De Rossi et al. 2017; Torrey et al. 2019; Langan et al. 2020; Ucci et al. 2023; Hirschmann et al. 2023).

Corresponding author: Danial Langeroodi
danial.langeroodi@nbi.ku.dk

Ground-based spectrographs have been used to probe the mass-metallicity relation out to $z \approx 3.5$, revealing a significant redshift evolution of its normalization (Sanders et al. 2015, 2021). At a fixed stellar mass, $z \approx 3.5$ galaxies are on average 2 – 3 times less metal enriched than those in the local Universe. Probing the mass-metallicity relation at higher redshifts with ground-based instruments becomes challenging since the rest-optical metallicity diagnostic lines get redshifted out of the atmospheric transmission window. At $z > 3$, ALMA-accessible far infrared [O III] $52\mu\text{m}$ and [O III] $88\mu\text{m}$ lines can be used as alternatives to rest-optical metallicity diagnostic lines (Jones et al. 2020). However, compiling large samples of such observations has proven challenging due to the required integration time and the lack of secure spectroscopically-confirmed targets. We note that this narrative will soon change since ALMA follow-ups of large samples of NIRSpect-confirmed $z > 3$ galaxies are currently underway.

JWST NIRSpect (Jakobsen et al. 2022) provides rest-optical spectroscopy for intermediate- to high-redshift galaxies out to $z \approx 10$. During the first cycle, this has already enabled new constraints on the mass-metallicity relation at $z > 3$ (e.g. Langeroodi et al. 2022; Heintz et al. 2022; Schaerer et al. 2022; Arellano-Córdova et al. 2022; Taylor et al. 2022; Trump et al. 2023; Rhoads et al. 2023; Curti et al. 2023a; Matthee et al. 2023; Nakajima et al. 2023; Curti et al. 2023b). Langeroodi et al. (2022) presented the first constraints on the mass-metallicity relation at $z \approx 8$, inferring significant evolution in its normalization with respect to the local Universe and a mild evolution with respect to the $z \approx 2 - 3$ constraints. Other studies exploiting larger samples of $z > 3$ galaxies compiled from the CEERS (Finkelstein et al. 2022a; Tang et al. 2023; Fujimoto et al. 2023) and JADES (Bunker et al. 2023) NIRSpect observations have probed the mass-metallicity relation at $z = 3 - 8$ (Nakajima et al. 2023; Curti et al. 2023b). A consistent picture is starting to emerge: there is a mild redshift evolution in the normalization of the mass-metallicity relation at $z > 3$, and the slope of the mass-metallicity relation seems to be flattening with increasing redshift.

The redshift evolution of the mass-metallicity relation out to $z \approx 3$ is consistently explained by the fundamental metallicity relation (FMR; see Andrews & Martini 2013; Curti et al. 2020). FMR refers to the empirically inferred anti-correlation between the gas-phase metallicity and the star-formation rate (SFR) at a fixed stellar mass. Since at fixed stellar mass, SFR increases with redshift (i.e. the redshift evolution of the star-formation main sequence; see e.g. Popesso et al. 2023), the FMR

results in a decline in the normalization of the mass-metallicity relation with increasing redshift.

There is no evidence for a redshift evolution of the FMR out to $z \approx 3$ (e.g. see Sanders et al. 2021). In other words, the FMR is fully capable of capturing the redshift evolution of the mass-metallicity relation out to $z \approx 3$. However, recent studies have shown that the FMR is starting to evolve at $z > 4$ (Heintz et al. 2022; Nakajima et al. 2022; Curti et al. 2023b). This evolution is typically shown in terms of the offset of the observed metallicities of high-redshift galaxies from the metallicities expected for their stellar masses and SFRs based on the local Universe calibrations of the FMR. High redshift galaxies appear more metal-poor than the FMR expectations given their stellar masses and SFRs. This indicates that the FMR is not fully capable of capturing the redshift evolution of the mass-metallicity relation at redshifts beyond $z \approx 4$.

The main mechanisms driving the redshift evolution of the FMR are not yet understood. However, there are speculations that the offset from the locally calibrated FMR is correlated with the compactness of galaxies. The main piece of evidence was presented in Tacchella et al. (2023), finding that the most metal-poor $z > 7$ galaxy detected in the Early Release Observations (Pontoppidan et al. 2022) data is very compact ($R_e < 200\text{pc}$). This galaxy has a high SFR surface density, potentially indicating that it is undergoing rapid/early-stage accretion, consistent with its inferred steeply rising SFH and relatively young stellar population. In this context, the offset from the FMR can be understood as the earliest stages of galaxy formation when the star formation is stochastic and equilibrium between gas infall, star formation, interstellar medium (ISM) enrichment, and feedback-driven outflow is not achieved yet. This equilibrium state is likely what we observe as the FMR for more mature galaxies at lower redshifts.

Here, we investigate the correlation between the offset from the FMR and compactness by compiling a large sample of $z > 3$ galaxies with available rest-optical NIRSpect spectroscopy as well as high-resolution NIRCams short-wavelength photometry. The former enables empirical method metallicity measurements and the latter enables accurate rest-ultraviolet (UV) size measurements. To compile this sample, we survey the entire publicly available *JWST* NIRSpect prism data, finding 334 galaxies at $z > 3$. We also leverage the first public data release of the JADES program (Bunker et al. 2023; Eisenstein et al. 2023; Hainline et al. 2023; Rieke & the JADES Collaboration 2023), providing an additional 93 galaxies at $z > 3$. The details of the public data used in

this work as well as our reduction routines are presented in Section 2.

We describe our methods for measuring the stellar masses, sizes, metallicities, and SFRs in Sections 3 and 4. In Section 5 we present the size measurements of our galaxies, highlighting the correlations between galaxy size, stellar mass, and redshift. In Section 6 we present our inference of the redshift evolution of the FMR and the correlation between the offset from the local FMR calibration and the compactness of galaxies. We discuss our findings and conclude in Sections 7 and 8.

Throughout this work we adopt a standard Λ CDM cosmology with $H_0 = 70 \text{ km s}^{-1} \text{ Mpc}^{-1}$, $\Omega_m = 0.3$, and $\Omega_\Lambda = 0.7$. Furthermore, we adopt a Chabrier (2003) stellar initial mass function (IMF), and magnitudes are in the AB system (Oke & Gunn 1983).

2. DATA

We surveyed the entire publicly available cycle 1 *JWST* data to find the $z_{\text{spec}} > 3$ galaxies covered by the prism disperser of the NIRSpec Multi-Object Spectroscopy (MOS) mode (Jakobsen et al. 2022; Ferruit et al. 2022; Böker et al. 2023) and imaged by NIRCcam (Rieke et al. 2005) and/or *HST*. We constructed a sample of 427 galaxies that have secure spectroscopic redshifts based on high signal-to-noise ratio (S/N) detections of the rest-optical metallicity diagnostic lines [O II] $\lambda\lambda 3727, 3729\text{\AA}$ doublet, H β , and [O III] $\lambda\lambda 4959, 5007\text{\AA}$ doublet. Our sample consists of 334 galaxies from public programs. In this Section, we provide an overview of the *JWST* and *HST* imaging and NIRSpec spectroscopy used in this work, as well as the routines deployed to reduce them. The remaining 93 galaxies were selected from the NIRCcam and NIRSpec public releases of the JADES program (Bunker et al. 2023; Eisenstein et al. 2023; Hainline et al. 2023; Rieke & the JADES Collaboration 2023).

2.1. Spectroscopy

The NIRSpec MOS prism data were obtained through programs 1345 (CEERS), 1433, 2750, 2756, and 2767. We retrieved the raw data products (`uncal.fits`) and micro-shutter assembly (MSA) files (`msa.fits`) from the Barbara A. Mikulski Archive for Space Telescopes (MAST)¹. We performed the detector-level corrections and converted the raw data into count-rate images (ramps-to-slopes) using the `Detector1Pipeline` routine of the official STScI *JWST* pipeline (Ferruit et al. 2022). We used the 1.10.0 version of the pipeline and

the `jwst_1077.pmap` Calibration Reference Data System (CRDS) context file.

The 2nd and 3rd reduction levels were carried out using the `msaexp` package (Brammer 2022)², which employs the official STScI pipeline with additional custom routines for further corrections. In particular, these routines pre-process the rate images to correct for the residual $1/f$ noise; detect and remove the “snowball” artifacts caused by large cosmic ray impacts; and remove bias, exposure by exposure. The WCS registration, flat-fielding, slit path-loss corrections, and flux calibration are performed using the `AssignWcs`, `Extract2dStep`, `FlatFieldStep`, `PathLossStep`, and `PhotomStep` routines from `Spec2Pipeline` module of the STScI pipeline.

The background is subtracted locally using a three-shutter node pattern before drizzling the background-subtracted images onto a common grid. `msaexp` extracts the optimal 1D spectra following the algorithm of Horne (1986) (Horne 1986): the 2D spectrum is integrated along the cross-dispersion axis; then the resulting signal along the spatial axis is fitted with a Gaussian profile to measure the spatial offset and aperture of the inverse-variance weighted kernel that extracts the optimal 1D spectrum.

We fitted the 1D spectra with `EAZY` (Brammer et al. 2008) to measure the spectroscopic redshifts. The fitted spectra were visually inspected to confirm the measured redshifts and to select the galaxies that satisfy the selection criteria mentioned above.

2.2. Photometry

The NIRCcam and *HST* photometry of the fields targeted by the NIRSpec MOS observations considered in this work were acquired from the Grizli Image Release (v6.0) repository³. This repository provides consistent reductions of the publicly available cycle 1 NIRCcam imaging as well as the ancillary *HST* data (G. Brammer 2023, in prep.). This includes mosaics of the EGS field (program 1345), as well as the fields toward lensing clusters Abell 2744 (programs 1324, 2561, and 2756), MACSJ0647 (program 1433), and RXJ2129 (program 2767). The NIRCcam photometry was calibrated using the `jwst_0995.pmap` CRDS context file. The stray-light features (i.e., “wisps”) were subtracted and the striping was removed using the `Grizli` software (Brammer 2019). All the NIRCcam and *HST* images were aligned to a common reference image and drizzled to the same 40 mas pixel grid.

² <https://github.com/gbrammer/msaexp>

³ <https://grizli.readthedocs.io/en/latest/grizli/image-release-v6.html>

¹ <https://mast.stsci.edu>

PSF-matching is required for measuring accurate source colors, unaffected by the filter/wavelength-dependent size of the PSF. For this purpose, we PSF-matched the imaging in every filter with a PSF FWHM below that of the F444W filter, to the PSF in this filter. For each field, the empirical PSF in each filter was constructed using the `PSFex` package (Bertin 2011). Potential stars were identified based on their location on the half-light-radius vs source magnitude plane, produced using the `Source Extractor` software (SE; Bertin & Arnouts 1996). The unsaturated stars were selected and pruned against significant contaminants as well as a high fraction of bad pixels. These stars were re-centered, stacked, and then normalized to construct the empirical PSFs. PSF-matching kernels from the bluer filters to F444W were produced following the *JWST* post-pipeline Data Analysis Tools Ecosystem routines⁴, and the mosaics in these bands were convolved to match the PSF in the F444W filter.

The PSF-matching procedure was not applied to the filters where PSF FWHM is larger than that of the F444W. This includes the NIRC*am* F480M filter as well as the *HST* WFC3_IR F105W, F110W, F125W, F140W, and F160W filters. We corrected the fluxes measured in *HST* WFC3_IR filters by multiplying them by a factor of 1.25 as suggested in Finkelstein et al. (2022b) (see also Finkelstein et al. 2022a), derived through source-injection simulations (note that this correction is specific to the *HST* WFC3_IR filters; below we apply another 1.08 correction to the flux measured in all the filters, which makes the overall correction consistent with the 1.35 factor reported in Finkelstein et al. 2022a).

The multi-band photometry of the spectroscopically selected galaxies in our final sample was measured in 0.3'' circular apertures (diameter) by running `SE` in dual-image mode. The detection and deblending criteria were set to `DETECT_MINAREA = 5`, `DETECT_THRESH = 3.0`, `DEBLEND_NTHRESH = 32`, `DEBLEND_MINCOUNT = 0.005`. The detection image in each field was constructed from the variance-weighted combination of the F277W, F356W, and F444W mosaics. In the few cases where the galaxy is not covered in NIRC*am* imaging, the F160W image was used for detection. For each galaxy, 1'' × 1'' cutouts of the detection image and segmentation map were visually inspected to ensure accurate detection and sufficient deblending.

We used the `MAG_APER` measurements on the PSF-matched images as the measured magnitudes and the

`MAGERR_APER` measurements on the original images (i.e., before PSF-matching) as their uncertainties. To perform aperture correction, we derived the correction factor for each galaxy as the ratio of the `MAG_AUTO` to `MAG_APER` flux in the F444W image. We scaled the measured `MAG_APER` values in all the filters by this factor to account for the flux that is not captured by the chosen aperture. We also corrected for the ~ 0.03 mag systematic offset between the `MAG_AUTO` values and the true total magnitudes, resulting from the wings of the PSF not being captured by the `MAG_AUTO` measurements (see, e.g., Finkelstein et al. 2022a). Moreover, to account for further uncertainties (e.g., zero points), we forced a noise floor of 10% on the measured magnitudes in each photometry band (see, e.g., Finkelstein et al. 2022a; Harikane et al. 2023).

We corrected for Galactic extinction using the E(B-V) reddening values from Schlafly & Finkbeiner (2011), assuming a Cardelli et al. (1989) attenuation curve. This corresponds to E(B-V) = 0.0089, 0.0112, 0.0966, and 0.0349 mag, respectively for the EGS, Abell 2744, MACSJ0647, and RXJ2129 fields. For each galaxy in the cluster fields, we corrected for lensing magnification given its sky location and spectroscopically measured redshift. We used the lensing models from Furtak et al. (2022) and Zitrin et al. (2015).

3. PHOTOMETRIC ANALYSIS

3.1. SED Fitting

We use the `prospector` software (Johnson et al. 2021) to derive the physical properties of the galaxies in our sample. `prospector` models the observed spectral energy distribution (SED) with synthetic spectra generated using the stellar population synthesis code `FSPS` (Conroy et al. 2009; Conroy & Gunn 2010), accessed through the `python` bindings of Foreman-Mackey et al. (2014). We adopt a similar `prospector` setup to what we used in Langeroodi et al. (2022) and Williams et al. (2023) for SED fitting of high-redshift galaxies with spectroscopically confirmed redshifts.

The redshift is fixed to the value measured based on emission lines and the star-formation history is modeled nonparametrically with 5 temporal bins (see Langeroodi et al. (2022) for the details of our temporal bin setup). Our stellar population free parameters include the total formed stellar mass, stellar metallicity, nebular metallicity, nebular ionization parameter, dust attenuation, and IGM attenuation. Adopting the model of Kriek & Conroy (2013), dust attenuation is fitted with a two-component model: a diffuse dust component for the entire galaxy and a birth-cloud component for the young

⁴ https://spacetelescope.github.io/jdat_notebooks/notebooks/NIRCcam_PSF-matched_photometry/NIRCcam_PSF_matched_multiband_photometry.html

stars. IGM attenuation is fitted with the redshift-dependent model of [Madau \(1995\)](#).

We use the built-in `dynesty` sampler ([Speagle 2020](#); [Koposov et al. 2022](#)) to explore the stellar population parameter space. `dynesty` adopts the dynamic nested sampling method developed by [Higson et al. \(2019\)](#). The weighted 1σ distributions of the last 10 percentiles of `dynesty` chains were used to infer the best-fit parameters.

3.2. Size Measurement

We measure galaxy sizes using the `galight` software ([Ding et al. 2020](#)), a wrapper around the `lenstronomy` image modeling tool ([Birrer et al. 2015](#); [Birrer & Amara 2018](#); [Birrer et al. 2021](#)) that automatically subtracts the sky background, identifies the bright objects in a given image cutout, and models them with user-specified light profiles. For simplicity, we model all the identified bright objects with Sersic profiles ([Sersic 1968](#)). [Kawinwanichakij et al. \(2021\)](#) and [Yang et al. \(2021\)](#) have demonstrated that half-light radii measured by `galight` are consistent with those measured by `galfit` ([Peng et al. 2002](#)).

We measure rest-UV sizes of the galaxies in our sample to target the extent of their star-forming regions. This choice was forced because, at the redshifts considered in this study, the rest-UV falls in the NIRCcam short wavelength filters with much better resolution and much smaller PSFs than the NIRCcam long wavelength filters. Hence, targeting the rest-UV enables more accurate size measurements. We model each galaxy in the broad-band filter that corresponds to rest-frame 2000 Å. This is mainly to ensure uniformity, and to avoid potential biases resulting from wavelength-dependent galaxy sizes. The downside is that this choice limits our analysis to galaxies at $z > 4$, below which the rest-frame 2000 Å falls in the NIRCcam F090W and shorter wavelength *HST* filters. The former does not cover a significant fraction of our sources and the latter does not provide a similar resolution to NIRCcam short-wavelength photometry.

Although we have constructed empirical PSFs for our entire sample (see Section 2.2), we chose to use `WebbPSF` ([Perrin et al. 2012, 2014](#)) PSFs for light profile modeling. This choice ensures that the sizes are measured consistently across our entire sample, especially given that the empirical PSF can be under-sampled for the fields which are covered in only a few NIRCcam pointings (e.g., programs 1433 and 2767). [Baggen et al. \(2023\)](#) have shown that the measured Sersic half-light radii are not sensitive to the choice of PSF and that the empirical and `WebbPSF` PSFs perform similarly.

4. SPECTRAL ANALYSIS

4.1. Emission Line Measurement

For each galaxy, we perform flux calibration by rescaling its spectrum to the measured photometry. The flux calibration factor is defined as the median ratio of the NIRCcam photometry and the photometry measured from the prism spectrum. The latter is measured using the `sedpy` package ([Johnson 2019](#)). We use the Penalized PiXel-Fitting package (`pPXF`; [Cappellari & Emsellem 2004](#); [Cappellari 2017, 2022](#)) to constrain the emission line fluxes on the calibrated spectra. `pPXF` simultaneously models the stellar continuum and emission by fitting the former with a stellar population and the latter with Gaussian profiles. We adopted the MILES stellar library ([Sánchez-Blázquez et al. 2006](#); [Falcón-Barroso et al. 2011](#)).

The measured line fluxes are corrected for Galactic extinction and lensing magnification following the prescriptions described in Section 2.1. We correct for intrinsic dust attenuation. If both the $H\beta$ and $H\alpha$ fluxes are constrained from the spectrum, the Balmer decrement (assuming Case B recombination; [Osterbrock 1989](#)) is used to correct the measured line fluxes. Otherwise, we use the A_V of the diffuse dust component, as inferred by SED fitting (see Section 3.1). We adopt a [Cardelli et al. \(1989\)](#) dust model.

We measure the SFR of each galaxy from its $H\alpha$ flux where available. We use the relation from [Calzetti \(2013\)](#) to convert the measured $H\alpha$ flux to SFR. At redshifts above $z \sim 7$, where $H\alpha$ falls out of the NIRSpc prism coverage, we use the $H\beta$ flux measurements to estimate the $H\alpha$ fluxes (assuming Case B recombination) and measure the SFRs. The measured SFRs are converted to Chabrier IMF ([Chabrier 2003](#)).

The adopted metallicity diagnostic method in this work (see Section 4.2) relies on the equivalent width of $H\beta$ ($EW_{H\beta}$) as a proxy for determining the ionization state of ISM. We measure $EW_{H\beta}$ using the best-fit Gaussian profile to $H\beta$ and the best-fit stellar continuum, both retrieved from the `pPXF` fits. The EW is measured in the wavelength range out of which the line flux has fallen below 0.01 of its peak flux.

4.2. Metallicity Measurement

We measure the gas-phase metallicities of the galaxies in our sample by closely following the empirical method detailed in [Nakajima et al. \(2022, 2023\)](#). We use the empirical emission line-metallicity calibrations from [Nakajima et al. \(2022\)](#), where the sensitivity of the calibration to the ionization state of ISM is taken into account by using $EW_{H\beta}$ as a proxy for the ionization state of ISM. Depending on the measured $EW_{H\beta}$, the correlation

between the line ratios and gas-phase metallicity is divided into three ionization state branches: $EW_{H\beta} < 100$, $100 < EW_{H\beta} < 200$, and $300 < EW_{H\beta}$. We use the $EW_{H\beta}$ values measured in Section 4.1 to decide which branch of the calibration applies to each galaxy.

For each galaxy, we use the R23⁵ ratio to determine its gas-phase metallicity. Each R23 ratio corresponds to two metallicity solutions. If these solutions are not sufficiently separated (i.e., they are within 1σ uncertainty of one another), we use the lower limit of the lower metallicity solution and the upper limit of the higher metallicity solution as the 1σ uncertainty region of the measured metallicity (with nominal value defined as the mean of the two solutions). If the two metallicity solutions are sufficiently separated, we use the monotonic O32⁶ ratio to differentiate between them. We chose the solution for which the expected O32 value is closer to the observed value. Objects for which R23 and O32 ratios could not be constrained with $S/N > 2$ are excluded from our analysis throughout the rest of this work. We note that in the low-metallicity regime (i.e. $12 + \log(O/H) < 7.6$), metallicities measured using the calibration of Nakajima et al. (2022) are in excellent agreement with those measured using the calibration of Izotov et al. (2019).

5. EVOLUTION OF GALAXY SIZES

5.1. Mass-Size Relation

Figure 1 shows the correlation between the UV size and the stellar mass of the $z_{\text{spec}} > 4$ galaxies in our sample (small green data points; see Section 3.2 for the motivations for the chosen redshift range). As expected from the luminosity-size relation inferred at lower and similar redshifts (see, e.g., Yang et al. 2021, 2022a,b), galaxy sizes are correlated with their stellar masses. The large orange data points show the weighted medians and 1σ distributions of the galaxies in our sample, in four bins of stellar mass. The dark purple line shows the best-fit least-squared power law, with a slope of 0.21 ± 0.04 and an intercept of 0.75 ± 0.38 .

The location of the lowest mass bin might indicate that the slope of the mass-size relation is flattening at the lower stellar mass end, especially below $\log(M_*/M_\odot) = 8$. However robust interpretations are limited by sample size at these stellar masses. The addition of more faint galaxies, e.g., those targeted by the deep pointing of JADES, can be instrumental in better understanding this potential flattening of the mass-size relation.

⁵ $([O\ III] \lambda\lambda 4959, 5007 + [O\ II] \lambda\lambda 3727, 29)/H\beta$

⁶ $[O\ III] \lambda 5007/[O\ II] \lambda\lambda 3727, 29$

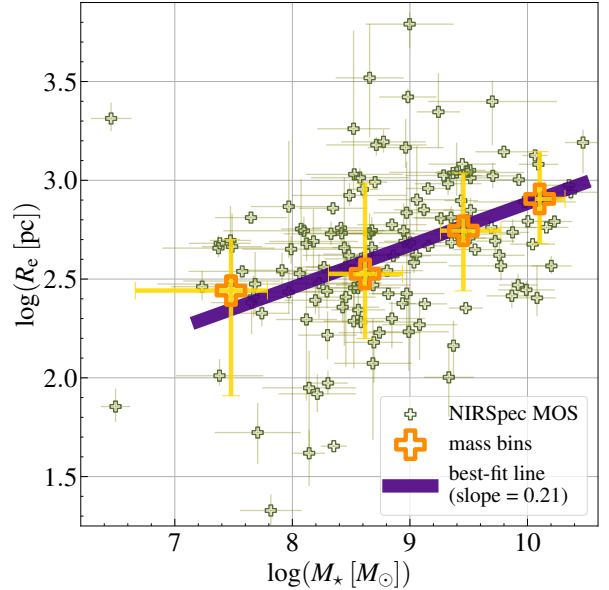


Figure 1. Mass-size relation at $z = 4 - 10$. The small green data points show the distribution of the stellar masses and UV sizes for the galaxies in our sample. The large orange data points show the weighted median and 1σ distributions in 4 bins of stellar mass. The dark purple line shows the best-fit power-law mass-size relation with a slope of 0.21 ± 0.04 . The offset of the lowest mass bin from the best-fit line (very) tentatively indicates the mass-size relation might be flattening at $\log(M_*/M_\odot) < 8$.

Interestingly, the highly magnified $z_{\text{spec}} = 9.51$ galaxy found behind the lensing cluster RXJ2129 (Williams et al. 2023) is the smallest and most compact entry in our sample; $R_e \sim 20\text{pc}$ and $\log(M_*/M_\odot) \sim 7.8$. We find a few new candidates potentially mimicking the massive compact ($\log(M_*/M_\odot) > 9.5$ and $R_e < 300\text{pc}$) galaxies found by Labbé et al. (2023) (see also Baggen et al. 2023). A detailed study of these galaxies is beyond the scope of this work.

5.2. Redshift Evolution of the Mass-Size Relation

Despite the relatively small uncertainties on the inferred slope of the mass-size relation ($\sim 19\%$; see Section 5.1), there is a significant scatter around the best-fit line. This is evident from the relatively large uncertainties on the inferred intercept of the mass-size relation ($\sim 50\%$), indicating that there is a large scatter in galaxy sizes at a fixed stellar mass. This signals that parameters other than the stellar mass play a role in shaping the mass-size relation.

Here, we consider the redshift evolution of the mass-size relation. Figure 2 shows the sizes of the galaxies in our sample plotted against their spectroscopic redshifts

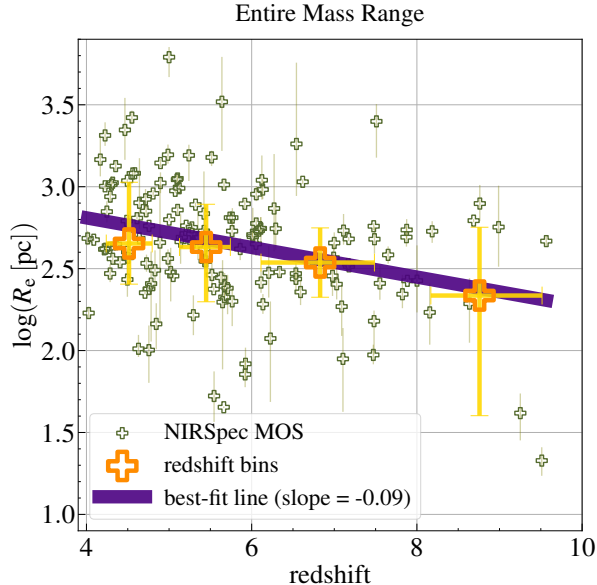


Figure 2. Redshift evolution of the mass-size relation. This Figure shows the sizes of the galaxies in our sample plotted against their spectroscopic redshifts (small green data points). The large orange data points show the weighted medians and 1σ distributions of the galaxies in our sample, in four redshift bins. There is a clear trend with redshift, where the sizes of galaxies on average get smaller with increasing redshift. The dark purple line shows the best-fit least-squared line with a slope of -0.090 ± 0.02 and an intercept of 3.17 ± 0.14 .

(small green data points). The large orange data points show the weighted medians and 1σ distributions of the galaxies in our sample, in four redshift bins. There is a clear trend with redshift, where the sizes of galaxies are on average getting smaller with increasing redshift. The dark purple line shows the best-fit least-squared line with a slope of -0.090 ± 0.02 and an intercept of 3.17 ± 0.14 .

Figure 2 and its size-redshift anti-correlation inference might be misleading. There are two mass-related systematics potentially affecting this inference. First, the number density of high-mass galaxies is expected to decline as a function of redshift. Therefore, the mass-size correlation (see Figure 1 and Section 5.1) implies that the average galaxy sizes for a complete sample are expected to decline at higher redshifts. Second, due to sensitivity limits the higher redshift samples are expected to be biased toward more massive/luminous galaxies. Due to the mass-size correlation, this can result in a flattening of the size-redshift relation. The described systematics work in opposite directions (i.e., one results in a steeper size-redshift anti-correlation and one flat-

tens the anti-correlation); however their combined effect cannot be neglected.

In order to mitigate the systematics described above, here we consider the size-redshift anti-correlation in bins of stellar mass. This is shown in Figure 3 where the upper-left panel corresponds to the $\log(M_*/M_\odot) < 8$ galaxies, upper-right panel to the $8 < \log(M_*/M_\odot) < 9$ galaxies, and the lower-left panel to the $9 < \log(M_*/M_\odot)$ galaxies. The large orange data points in each panel show the medians and 1σ distributions of the sample, in bins of redshift. The dark purple line in each panel shows the best-fit least-squared size-redshift relation in the corresponding stellar mass bin; the best-fit slopes and their uncertainties are noted at the bottom of each panel.

Figure 3 presents a consistent picture. Galaxies are more compact at higher redshifts. The strength of this redshift evolution seems to depend on stellar mass. The lowest stellar mass galaxies ($\log(M_*/M_\odot) < 8$) exhibit the steepest redshift evolution, while the sizes of highest stellar mass galaxies ($9 < \log(M_*/M_\odot)$) does not seem to evolve with redshift.

6. FUNDAMENTAL METALLICITY RELATION

In this Section, we investigate the redshift evolution of the FMR (Section 6.1) and its correlation with the compactness of high-redshift galaxies (Section 6.2). For each galaxy in our sample, we use the FMR calibration from Andrews & Martini (2013) to derive the expected gas-phase metallicity for its stellar mass (measured by SED fitting; Sections 3.1) and SFR (measured from $H\alpha$ or $H\beta$; Section 4.1). We use the formulation provided in Nakajima et al. (2023), where the calibration of Andrews & Martini (2013) is converted from the Kroupa IMF to the Chabrier IMF

$$12 + \log(\text{O}/\text{H}) = 0.43 \times \mu_{0.66} + 4.58; \quad (1)$$

$$\text{where } \mu_\alpha = \log M_* - \alpha \log \text{SFR}. \quad (2)$$

6.1. (mild) Redshift Evolution of the FMR

Figure 4 shows the mild redshift evolution of the FMR. The offsets ($\log(\text{O}/\text{H})_{\text{obs}} - \log(\text{O}/\text{H})_{\text{FMR}}$) between the measured metallicities and the metallicities expected from the locally calibrated FMR consistently increase as a function of redshift. We note that the measured offset strongly depends on the adopted FMR calibration. For instance, as shown in Nakajima et al. (2023), adopting the calibration from Curti et al. (2020) results in more significant offsets across the entire redshift range.

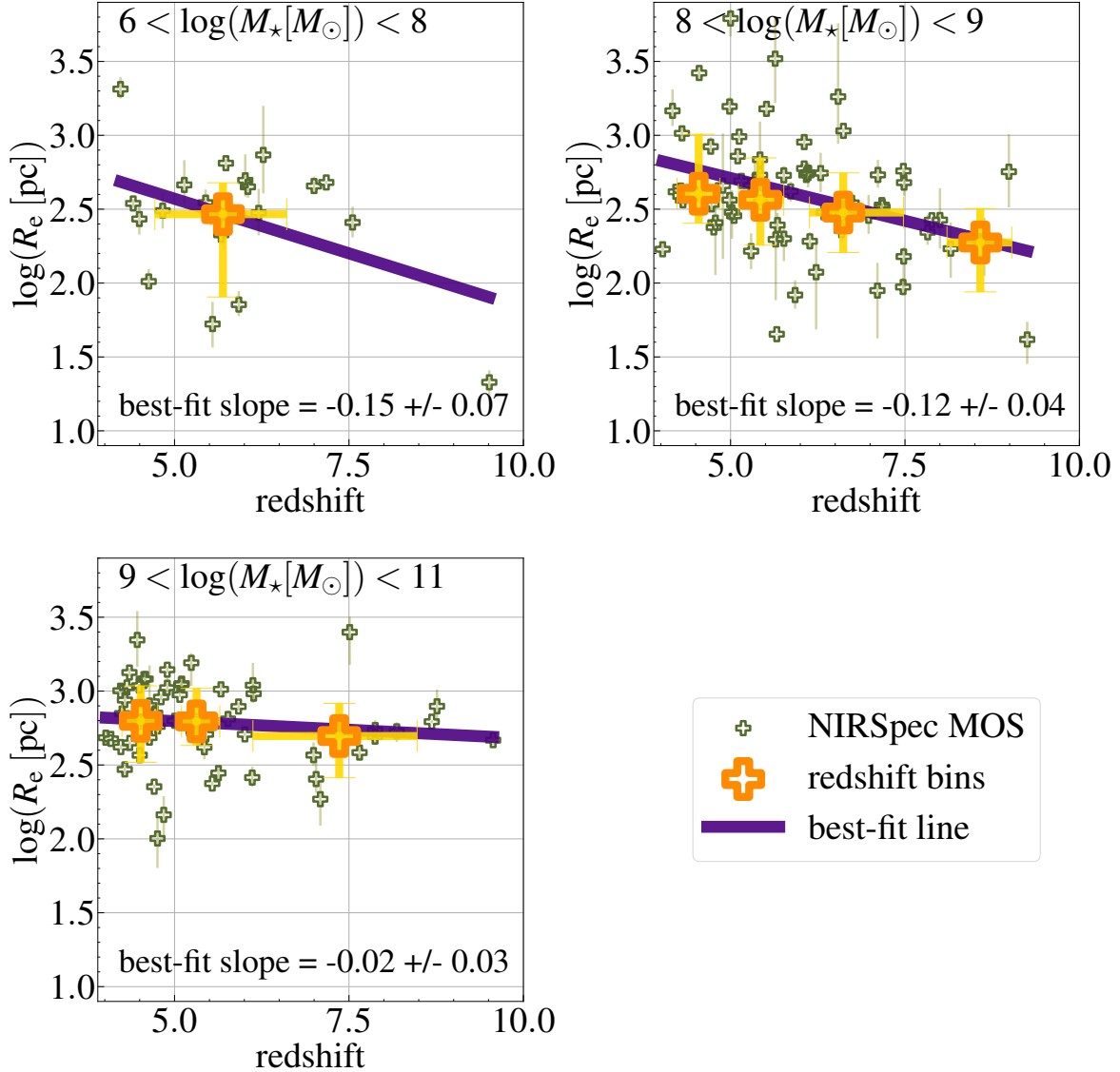


Figure 3. Redshift evolution of the mass-size relation in bins of stellar mass. Each panel shows the evolution of galaxy sizes as a function of redshift in its corresponding stellar mass bin (as indicated on top of the panel). The small green data points show the individual galaxies in our sample. The large orange data points show the weighted medians and 1σ distributions in bins of redshift. The dark purple lines show the best-fit size-redshift linear relations, with their slopes noted on the bottom of the corresponding panel. The lowest-mass galaxies ($\log(M_*/M_\odot) < 8$; upper-left panel) show the strongest size-redshift evolution, while the highest-mass galaxies ($9 < \log(M_*/M_\odot)$; lower-left panel) show no redshift evolution.

Nonetheless, as shown in both Nakajima et al. (2023) and Curti et al. (2023b), the mild redshift evolution of the offset from the locally calibrated FMR persists.

Moreover, we note that the inferred offsets are sensitive to the adopted empirical metallicity calibration. For instance, using the calibration from Sanders et al. (2023) results in generally higher offsets (in the same direction as Figure 4) as well as larger scatter in the offsets. Adopting the calibration from Izotov et al. (2019)

for $12 + \log(\text{O}/\text{H}) < 7.6$ galaxies (the metallicity range where this calibration is valid) results in offsets that are similar to what is shown in Figure 4 but with much lower scatter. Nonetheless, in both scenarios, the redshift evolution persists.

6.2. FMR Offset vs Compactness

In Figure 5, we present the FMR offsets of the galaxies in our sample plotted against their “compactness”

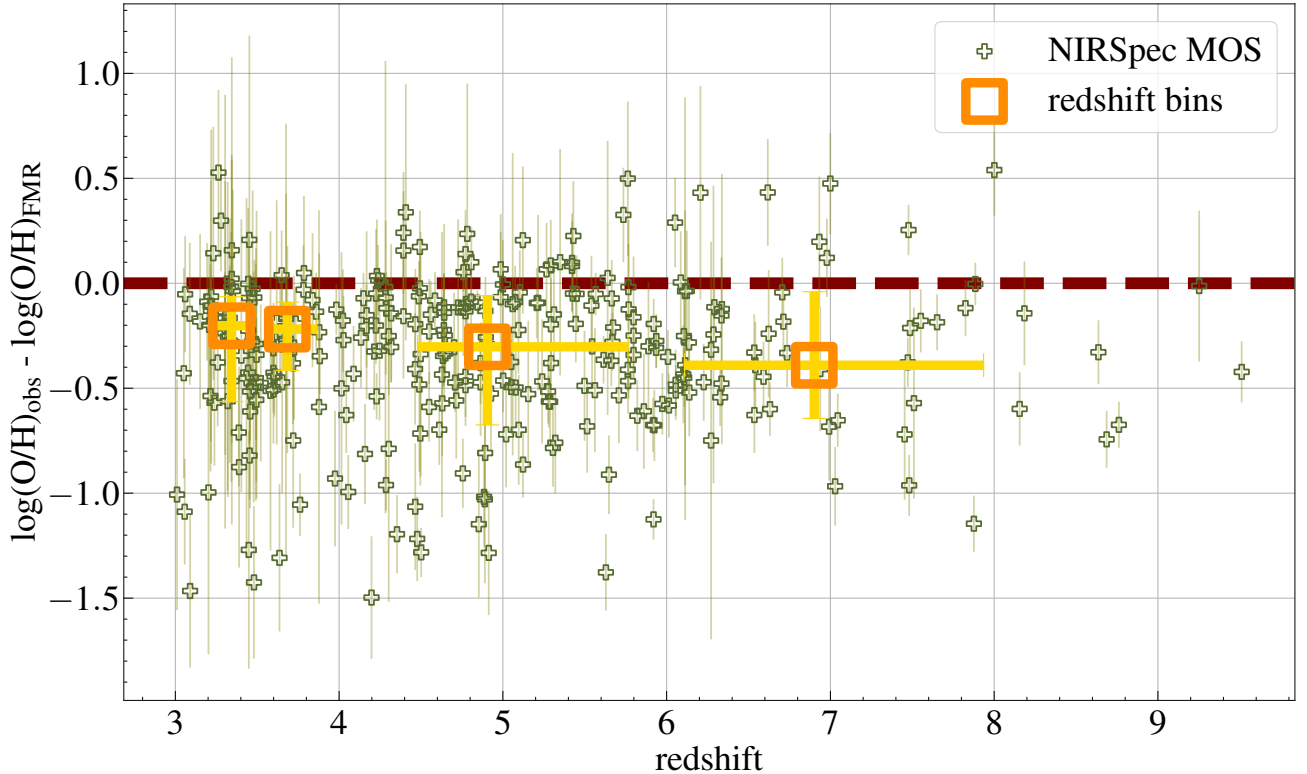


Figure 4. Redshift evolution of the fundamental metallicity relation. The small green data points show the offset of the measured metallicities for the galaxies in our sample from the FMR expectation for their stellar mass and SFR. The large orange data points show the weighted median and 1σ standard deviations in bins of redshift. The dashed red line indicates zero offsets from the locally calibrated FMR. There is a mild redshift evolution in the FMR.

(small green data points). The compactness is defined as

$$\text{compactness} := \kappa \times \log(M_{\star} [M_{\odot}]) - \log(R_e [\text{pc}]), \quad (3)$$

where κ is the slope of the mass-size power-law relation (see Figure 1 and Section 5.1). The compactness parameter measures if the galaxy is more compact than expected for its stellar mass. In other words, it correlates with downward deviations from the mass-size relation. We set $\kappa = 0.21$, based on the best-fit mass-size relation derived in Section 6.2. The large orange data points correspond to the weighted medians and 1σ scatters of the galaxies in our sample, in three bins of compactness.

Figure 5 shows that the FMR offset and compactness are correlated. We fit (least-squared) this correlation with a linear relation, inferring a best-fit slope of -0.35 ± 0.11 and an intercept of -0.56 ± 0.09 . This is shown as the dark purple line in Figure 5. This correlation indicates that as galaxies get more compact at a fixed stellar mass and SFR, they become more metal-poor.

We discuss the implications of this finding in the next Section.

7. DISCUSSION

7.1. Inside-Out Star Formation in Simplest High- z Galaxies

Figure 5 shows that as galaxies get more rest-UV compact (i.e. moving along the x-axis) they become more metal-deficient (i.e. moving opposite to the y-axis). The rest-UV compactness of young high-redshift galaxies can be attributed to a recent infall of low-metallicity/pristine gas that has ignited star formation only in the most central regions of the galaxy. The recent accretion is evident from the systematically low gas-phase metallicity of these compact galaxies.

We are likely observing these galaxies at the very early stages of gas accretion when enough time has not passed to allow the galaxy to exhibit a more widespread star formation. This can provide evidence for an inside-out star-formation scenario, where the simplest high redshift galaxies form the bulk of their stellar mass in a centrally-concentrated burst of star formation. Following this first

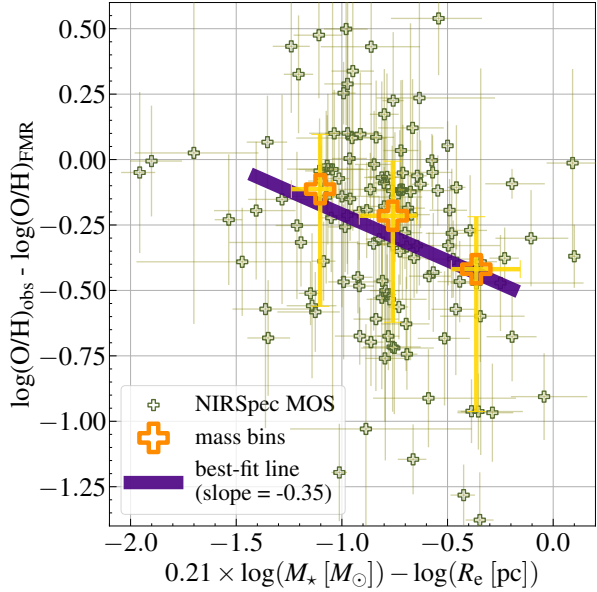


Figure 5. Compact galaxies are more metal-deficient. The small green data points show the offset from the locally calibrated FMR as a function of compactness (defined as $0.21 \times \log(M_\star [M_\odot]) - \log(R_e [\text{pc}])$; see text). The large orange data points show the weighted median and 1σ distributions in bins of compactness. As the galaxies become more compact (i.e. moving along the x-axis) they become more offset from the locally calibrated FMR corresponding to lower gas-phase metallicities.

burst of star formation and the formation of a core, the stellar feedback from the core starts to prohibit further centrally concentrated star formation. This can force the later star-formation episodes to spread further from the core, resulting in less compact galaxies at later times.

This picture is supported by Section 5.2 and Figures 2 and 3, where we present the redshift evolution of the mass-size relation. In particular, Figure 3 shows that at a fixed stellar mass, higher redshift galaxies are more compact. In order to build up their stellar mass, higher redshift galaxies have to undergo more rapid accretion and bursty star formation compared to lower redshift galaxies of the same stellar mass which have had enough time to undergo longer episodes of slower accretion and star formation. As a result, high-redshift galaxies can on average appear more compact than their low-redshift counterparts.

The rapid episodes of accretion can be attributed to stochastic star formation. High-redshift galaxies are more compact (see Figures 2 and 3) than low-redshift galaxies of the same stellar mass. In particular, Figure 3 shows that the sizes of lower-stellar mass galaxies experience a more severe redshift evolution. This suggests

that stochastic star formation is a more dominant mode of star formation for lower stellar mass galaxies.

7.2. FMR as a State of Equilibrium

The systematically low ISM metallicities of these compact galaxies indicate that their gas infall happens on timescales that are much shorter than what is needed for the newly formed generation of massive stars to dilute the ISM. Each star formation episode is followed by an episode of supernovae enrichment with a delay of $> 10^{5.5}\text{yr}$, corresponding to the lifetime of the most massive supernovae progenitors. In this context, the offset from the FMR provides an unexplored avenue for constraining the timescales of accretion, star formation, and stellar feedback to better understand the formation and evolution of the first galaxies.

The FMR can be considered an equilibrium state attained much later than the accretion and burst of star formation. In this context, the offset from the FMR indicates that the galaxy has not reached equilibrium yet. Stochastic star formation episodes, characterized by short and rapid phases of accretion can cause this far from equilibrium state (see Section 7.1). The offset from the FMR is increasing as a function of redshift, indicating that stochastic star formation becomes a more dominant mode at higher redshift.

8. CONCLUSION

We compile a sample of 427 $z > 3$ galaxies covered by both the NIRSpec prism and NIRCам short-wavelength photometry, consisting of 334 galaxies from the publicly available programs and 93 galaxies from the first data release of the JADES program. We measure the stellar masses, sizes, SFRs, and gas-phase metallicities of these galaxies to investigate the anti-correlation between the gas-phase metallicity and compactness.

We infer the mass-size relation at $z = 4 - 10$, best-fitted with a power-law with a slope of 0.21 ± 0.04 . We investigate the redshift evolution of the mass-size relation, finding that at a fixed stellar mass, higher redshift galaxies appear more compact. The degree of this redshift evolution depends on the stellar mass, with the lowest mass galaxies showing the strongest redshift evolution and the most massive galaxies ($\log(M_\star/M_\odot) > 9$) showing no redshift evolution.

We find that the more compact galaxies appear more metal poor, suggesting that they are undergoing more rapid phases of gas infall and star formation. This suggests that stochastic star formation becomes a more dominant mode of star formation at higher redshifts. The centrally concentrated bursts of star formation in these compact metal-deficient galaxies favours an inside-out star formation scenario, where the cores are formed

early on through a centrally concentrated burst of star formation.

The offset from the FMR for these compact galaxies suggest that they are out of equilibrium, meaning that their accretion and star formation timescales have been much shorter than the enrichment and stellar feedback timescales. Metal deficiency and the offset from the FMR can be considered a signature for stochastic star formation.

9. ACKNOWLEDGMENT

D.L. greatly appreciates helpful discussions with Mirko Curti, Kimihiko Nakajima, and Ryan Sanders which influenced some of the interpretations and conclusions in this work. We are thankful for the technical comments by Pablo Pérez-González on PSF-matching and flux uncertainty measurements. We are indebted to

Gabe Brammer for making his *JWST/HST* image reductions publicly available. We acknowledge the clear description of the post-pipeline NIRCcam photometry analysis by the CEERS team and Yuichi Harikane in their respective papers, without which those steps of this work would have become much more challenging. D.L. and J.H. were supported by a VILLUM FONDEN Investigator grant (project number 16599).

Software: dynesty (Speagle 2020), EAZY (Brammer et al. 2008), FSPS (Conroy et al. 2009; Conroy & Gunn 2010), galight (Ding et al. 2020), Grizli (Brammer 2019), msaexp (Brammer 2022), pPXF (Cappellari & Emsellem 2004; Cappellari 2017, 2022), PSFex (Bertin 2011), prospector (Johnson et al. 2021), sedpy (Johnson 2019), Source Extractor (Bertin & Arnouts 1996), WebbPSF (Perrin et al. 2012, 2014)

REFERENCES

- Andrews, B. H., & Martini, P. 2013, *ApJ*, 765, 140, doi: [10.1088/0004-637X/765/2/140](https://doi.org/10.1088/0004-637X/765/2/140)
- Arellano-Córdova, K. Z., Berg, D. A., Chisholm, J., et al. 2022, *ApJL*, 940, L23, doi: [10.3847/2041-8213/ac9ab2](https://doi.org/10.3847/2041-8213/ac9ab2)
- Baggen, J. F. W., van Dokkum, P., Labbe, I., et al. 2023, arXiv e-prints, arXiv:2305.17162, doi: [10.48550/arXiv.2305.17162](https://doi.org/10.48550/arXiv.2305.17162)
- Bertin, E. 2011, in *Astronomical Society of the Pacific Conference Series*, Vol. 442, *Astronomical Data Analysis Software and Systems XX*, ed. I. N. Evans, A. Accomazzi, D. J. Mink, & A. H. Rots, 435
- Bertin, E., & Arnouts, S. 1996, *A&AS*, 117, 393, doi: [10.1051/aas:1996164](https://doi.org/10.1051/aas:1996164)
- Birrer, S., & Amara, A. 2018, *Physics of the Dark Universe*, 22, 189, doi: [10.1016/j.dark.2018.11.002](https://doi.org/10.1016/j.dark.2018.11.002)
- Birrer, S., Amara, A., & Refregier, A. 2015, *ApJ*, 813, 102, doi: [10.1088/0004-637X/813/2/102](https://doi.org/10.1088/0004-637X/813/2/102)
- Birrer, S., Shajib, A., Gilman, D., et al. 2021, *The Journal of Open Source Software*, 6, 3283, doi: [10.21105/joss.03283](https://doi.org/10.21105/joss.03283)
- Böker, T., Beck, T. L., Birkmann, S. M., et al. 2023, *PASP*, 135, 038001, doi: [10.1088/1538-3873/acb846](https://doi.org/10.1088/1538-3873/acb846)
- Brammer, G. 2019, Grizli: Grism redshift and line analysis software, *Astrophysics Source Code Library*, record ascl:1905.001. <http://ascl.net/1905.001>
- . 2022, msaexp: NIRSpc analysis tools, 0.3.4, Zenodo, Zenodo, doi: [10.5281/zenodo.7299500](https://doi.org/10.5281/zenodo.7299500)
- Brammer, G. B., van Dokkum, P. G., & Coppi, P. 2008, *ApJ*, 686, 1503, doi: [10.1086/591786](https://doi.org/10.1086/591786)
- Bunker, A. J., Cameron, A. J., Curtis-Lake, E., et al. 2023, arXiv e-prints, arXiv:2306.02467, doi: [10.48550/arXiv.2306.02467](https://doi.org/10.48550/arXiv.2306.02467)
- Calzetti, D. 2013, in *Secular Evolution of Galaxies*, ed. J. Falcón-Barroso & J. H. Knapen, 419, doi: [10.48550/arXiv.1208.2997](https://doi.org/10.48550/arXiv.1208.2997)
- Cappellari, M. 2017, *MNRAS*, 466, 798, doi: [10.1093/mnras/stw3020](https://doi.org/10.1093/mnras/stw3020)
- . 2022, *MNRAS* submitted, doi: [10.48550/arXiv.2208.14974](https://doi.org/10.48550/arXiv.2208.14974)
- Cappellari, M., & Emsellem, E. 2004, *PASP*, 116, 138, doi: [10.1086/381875](https://doi.org/10.1086/381875)
- Cardelli, J. A., Clayton, G. C., & Mathis, J. S. 1989, *ApJ*, 345, 245, doi: [10.1086/167900](https://doi.org/10.1086/167900)
- Chabrier, G. 2003, *PASP*, 115, 763, doi: [10.1086/376392](https://doi.org/10.1086/376392)
- Conroy, C., & Gunn, J. E. 2010, *ApJ*, 712, 833, doi: [10.1088/0004-637X/712/2/833](https://doi.org/10.1088/0004-637X/712/2/833)
- Conroy, C., Gunn, J. E., & White, M. 2009, *ApJ*, 699, 486, doi: [10.1088/0004-637X/699/1/486](https://doi.org/10.1088/0004-637X/699/1/486)
- Curti, M., Mannucci, F., Cresci, G., & Maiolino, R. 2020, *MNRAS*, 491, 944, doi: [10.1093/mnras/stz2910](https://doi.org/10.1093/mnras/stz2910)
- Curti, M., D’Eugenio, F., Carniani, S., et al. 2023a, *MNRAS*, 518, 425, doi: [10.1093/mnras/stac2737](https://doi.org/10.1093/mnras/stac2737)
- Curti, M., Maiolino, R., Carniani, S., et al. 2023b, arXiv e-prints, arXiv:2304.08516, doi: [10.48550/arXiv.2304.08516](https://doi.org/10.48550/arXiv.2304.08516)
- De Rossi, M. E., Bower, R. G., Font, A. S., Schaye, J., & Theuns, T. 2017, *MNRAS*, 472, 3354, doi: [10.1093/mnras/stx2158](https://doi.org/10.1093/mnras/stx2158)
- Ding, X., Silverman, J., Treu, T., et al. 2020, *ApJ*, 888, 37, doi: [10.3847/1538-4357/ab5b90](https://doi.org/10.3847/1538-4357/ab5b90)

- Eisenstein, D. J., Willott, C., Alberts, S., et al. 2023, arXiv e-prints, arXiv:2306.02465, doi: [10.48550/arXiv.2306.02465](https://doi.org/10.48550/arXiv.2306.02465)
- Falcón-Barroso, J., Sánchez-Blázquez, P., Vazdekis, A., et al. 2011, *A&A*, 532, A95, doi: [10.1051/0004-6361/201116842](https://doi.org/10.1051/0004-6361/201116842)
- Ferruit, P., Jakobsen, P., Giardino, G., et al. 2022, *A&A*, 661, A81, doi: [10.1051/0004-6361/202142673](https://doi.org/10.1051/0004-6361/202142673)
- Finkelstein, S. L., Bagley, M. B., Ferguson, H. C., et al. 2022a, arXiv e-prints, arXiv:2211.05792, doi: [10.48550/arXiv.2211.05792](https://doi.org/10.48550/arXiv.2211.05792)
- Finkelstein, S. L., Bagley, M., Song, M., et al. 2022b, *ApJ*, 928, 52, doi: [10.3847/1538-4357/ac3aed](https://doi.org/10.3847/1538-4357/ac3aed)
- Foreman-Mackey, D., Sick, J., & Johnson, B. 2014, python-fsps: Python bindings to FSPS (v0.1.1), v0.1.1, Zenodo, Zenodo, doi: [10.5281/zenodo.12157](https://doi.org/10.5281/zenodo.12157)
- Fujimoto, S., Arrabal Haro, P., Dickinson, M., et al. 2023, *ApJL*, 949, L25, doi: [10.3847/2041-8213/acd2d9](https://doi.org/10.3847/2041-8213/acd2d9)
- Furtak, L. J., Zitrin, A., Weaver, J. R., et al. 2022, arXiv e-prints, arXiv:2212.04381, doi: [10.48550/arXiv.2212.04381](https://doi.org/10.48550/arXiv.2212.04381)
- Hainline, K. N., Johnson, B. D., Robertson, B., et al. 2023, arXiv e-prints, arXiv:2306.02468, doi: [10.48550/arXiv.2306.02468](https://doi.org/10.48550/arXiv.2306.02468)
- Harikane, Y., Ouchi, M., Oguri, M., et al. 2023, *ApJS*, 265, 5, doi: [10.3847/1538-4365/acaaa5](https://doi.org/10.3847/1538-4365/acaaa5)
- Heintz, K. E., Brammer, G. B., Giménez-Arteaga, C., et al. 2022, arXiv e-prints, arXiv:2212.02890, doi: [10.48550/arXiv.2212.02890](https://doi.org/10.48550/arXiv.2212.02890)
- Higson, E., Handley, W., Hobson, M., & Lasenby, A. 2019, *Statistics and Computing*, 29, 891, doi: [10.1007/s11222-018-9844-0](https://doi.org/10.1007/s11222-018-9844-0)
- Hirschmann, M., Charlot, S., & Somerville, R. S. 2023, arXiv e-prints, arXiv:2305.03753, doi: [10.48550/arXiv.2305.03753](https://doi.org/10.48550/arXiv.2305.03753)
- Hirschmann, M., De Lucia, G., & Fontanot, F. 2016, *MNRAS*, 461, 1760, doi: [10.1093/mnras/stw1318](https://doi.org/10.1093/mnras/stw1318)
- Horne, K. 1986, *PASP*, 98, 609, doi: [10.1086/131801](https://doi.org/10.1086/131801)
- Izotov, Y. I., Guseva, N. G., Fricke, K. J., & Henkel, C. 2019, *A&A*, 623, A40, doi: [10.1051/0004-6361/201834768](https://doi.org/10.1051/0004-6361/201834768)
- Jakobsen, P., Ferruit, P., Alves de Oliveira, C., et al. 2022, *A&A*, 661, A80, doi: [10.1051/0004-6361/202142663](https://doi.org/10.1051/0004-6361/202142663)
- Johnson, B. D. 2019, SEDPY: Modules for storing and operating on astronomical source spectral energy distribution, *Astrophysics Source Code Library*, record ascl:1905.026. <http://ascl.net/1905.026>
- Johnson, B. D., Leja, J., Conroy, C., & Speagle, J. S. 2021, *ApJS*, 254, 22, doi: [10.3847/1538-4365/abef67](https://doi.org/10.3847/1538-4365/abef67)
- Jones, T., Sanders, R., Roberts-Borsani, G., et al. 2020, *ApJ*, 903, 150, doi: [10.3847/1538-4357/abb943](https://doi.org/10.3847/1538-4357/abb943)
- Kawinwanichakij, L., Silverman, J. D., Ding, X., et al. 2021, *ApJ*, 921, 38, doi: [10.3847/1538-4357/ac1f21](https://doi.org/10.3847/1538-4357/ac1f21)
- Koposov, S., Speagle, J., Barbary, K., et al. 2022, joshspeagle/dynesty: v1.2.3, v1.2.3, Zenodo, Zenodo, doi: [10.5281/zenodo.6609296](https://doi.org/10.5281/zenodo.6609296)
- Kriek, M., & Conroy, C. 2013, *ApJL*, 775, L16, doi: [10.1088/2041-8205/775/1/L16](https://doi.org/10.1088/2041-8205/775/1/L16)
- Labbé, I., van Dokkum, P., Nelson, E., et al. 2023, *Nature*, 616, 266, doi: [10.1038/s41586-023-05786-2](https://doi.org/10.1038/s41586-023-05786-2)
- Lagos, C. d. P., Theuns, T., Schaye, J., et al. 2016, *MNRAS*, 459, 2632, doi: [10.1093/mnras/stw717](https://doi.org/10.1093/mnras/stw717)
- Langan, I., Ceverino, D., & Finlator, K. 2020, *MNRAS*, 494, 1988, doi: [10.1093/mnras/staa880](https://doi.org/10.1093/mnras/staa880)
- Langeroodi, D., Hjorth, J., Chen, W., et al. 2022, arXiv e-prints, arXiv:2212.02491, doi: [10.48550/arXiv.2212.02491](https://doi.org/10.48550/arXiv.2212.02491)
- Ma, X., Hopkins, P. F., Faucher-Giguère, C.-A., et al. 2016, *MNRAS*, 456, 2140, doi: [10.1093/mnras/stv2659](https://doi.org/10.1093/mnras/stv2659)
- Madau, P. 1995, *ApJ*, 441, 18, doi: [10.1086/175332](https://doi.org/10.1086/175332)
- Matthee, J., Mackenzie, R., Simcoe, R. A., et al. 2023, *ApJ*, 950, 67, doi: [10.3847/1538-4357/acc846](https://doi.org/10.3847/1538-4357/acc846)
- Nakajima, K., Ouchi, M., Isobe, Y., et al. 2023, arXiv e-prints, arXiv:2301.12825, doi: [10.48550/arXiv.2301.12825](https://doi.org/10.48550/arXiv.2301.12825)
- Nakajima, K., Ouchi, M., Xu, Y., et al. 2022, *ApJS*, 262, 3, doi: [10.3847/1538-4365/ac7710](https://doi.org/10.3847/1538-4365/ac7710)
- Oke, J. B., & Gunn, J. E. 1983, *ApJ*, 266, 713, doi: [10.1086/160817](https://doi.org/10.1086/160817)
- Osterbrock, D. E. 1989, *Astrophysics of gaseous nebulae and active galactic nuclei*
- Peng, C. Y., Ho, L. C., Impey, C. D., & Rix, H.-W. 2002, *AJ*, 124, 266, doi: [10.1086/340952](https://doi.org/10.1086/340952)
- Perrin, M. D., Sivaramakrishnan, A., Lajoie, C.-P., et al. 2014, in *Society of Photo-Optical Instrumentation Engineers (SPIE) Conference Series*, Vol. 9143, *Space Telescopes and Instrumentation 2014: Optical, Infrared, and Millimeter Wave*, ed. J. Oschmann, Jacobus M., M. Clampin, G. G. Fazio, & H. A. MacEwen, 91433X, doi: [10.1117/12.2056689](https://doi.org/10.1117/12.2056689)
- Perrin, M. D., Soummer, R., Elliott, E. M., Lallo, M. D., & Sivaramakrishnan, A. 2012, in *Society of Photo-Optical Instrumentation Engineers (SPIE) Conference Series*, Vol. 8442, *Space Telescopes and Instrumentation 2012: Optical, Infrared, and Millimeter Wave*, ed. M. C. Clampin, G. G. Fazio, H. A. MacEwen, & J. Oschmann, Jacobus M., 84423D, doi: [10.1117/12.925230](https://doi.org/10.1117/12.925230)
- Pontoppidan, K. M., Barrientes, J., Blome, C., et al. 2022, *ApJL*, 936, L14, doi: [10.3847/2041-8213/ac8a4e](https://doi.org/10.3847/2041-8213/ac8a4e)
- Popesso, P., Concas, A., Cresci, G., et al. 2023, *MNRAS*, 519, 1526, doi: [10.1093/mnras/stac3214](https://doi.org/10.1093/mnras/stac3214)

- Rhoads, J. E., Wold, I. G. B., Harish, S., et al. 2023, *ApJL*, 942, L14, doi: [10.3847/2041-8213/acaaf](https://doi.org/10.3847/2041-8213/acaaf)
- Rieke, M., & the JADES Collaboration. 2023, arXiv e-prints, arXiv:2306.02466, doi: [10.48550/arXiv.2306.02466](https://doi.org/10.48550/arXiv.2306.02466)
- Rieke, M. J., Kelly, D., & Horner, S. 2005, in *Society of Photo-Optical Instrumentation Engineers (SPIE) Conference Series*, Vol. 5904, *Cryogenic Optical Systems and Instruments XI*, ed. J. B. Heaney & L. G. Burriesci, 1–8, doi: [10.1117/12.615554](https://doi.org/10.1117/12.615554)
- Sánchez-Blázquez, P., Peletier, R. F., Jiménez-Vicente, J., et al. 2006, *MNRAS*, 371, 703, doi: [10.1111/j.1365-2966.2006.10699.x](https://doi.org/10.1111/j.1365-2966.2006.10699.x)
- Sanders, R. L., Shapley, A. E., Topping, M. W., Reddy, N. A., & Brammer, G. B. 2023, arXiv e-prints, arXiv:2303.08149, doi: [10.48550/arXiv.2303.08149](https://doi.org/10.48550/arXiv.2303.08149)
- Sanders, R. L., Shapley, A. E., Kriek, M., et al. 2015, *ApJ*, 799, 138, doi: [10.1088/0004-637X/799/2/138](https://doi.org/10.1088/0004-637X/799/2/138)
- Sanders, R. L., Shapley, A. E., Jones, T., et al. 2021, *ApJ*, 914, 19, doi: [10.3847/1538-4357/abf4c1](https://doi.org/10.3847/1538-4357/abf4c1)
- Schaerer, D., Marques-Chaves, R., Barrufet, L., et al. 2022, *A&A*, 665, L4, doi: [10.1051/0004-6361/202244556](https://doi.org/10.1051/0004-6361/202244556)
- Schaye, J., Crain, R. A., Bower, R. G., et al. 2015, *MNRAS*, 446, 521, doi: [10.1093/mnras/stu2058](https://doi.org/10.1093/mnras/stu2058)
- Schlafly, E. F., & Finkbeiner, D. P. 2011, *ApJ*, 737, 103, doi: [10.1088/0004-637X/737/2/103](https://doi.org/10.1088/0004-637X/737/2/103)
- Sersic, J. L. 1968, *Atlas de Galaxias Australes*
- Speagle, J. S. 2020, *MNRAS*, 493, 3132, doi: [10.1093/mnras/staa278](https://doi.org/10.1093/mnras/staa278)
- Tacchella, S., Johnson, B. D., Robertson, B. E., et al. 2023, *MNRAS*, 522, 6236, doi: [10.1093/mnras/stad1408](https://doi.org/10.1093/mnras/stad1408)
- Tang, M., Stark, D. P., Chen, Z., et al. 2023, arXiv e-prints, arXiv:2301.07072, doi: [10.48550/arXiv.2301.07072](https://doi.org/10.48550/arXiv.2301.07072)
- Taylor, A. J., Barger, A. J., & Cowie, L. L. 2022, *ApJL*, 939, L3, doi: [10.3847/2041-8213/ac959d](https://doi.org/10.3847/2041-8213/ac959d)
- Torrey, P., Vogelsberger, M., Marinacci, F., et al. 2019, *MNRAS*, 484, 5587, doi: [10.1093/mnras/stz243](https://doi.org/10.1093/mnras/stz243)
- Trump, J. R., Arrabal Haro, P., Simons, R. C., et al. 2023, *ApJ*, 945, 35, doi: [10.3847/1538-4357/acba8a](https://doi.org/10.3847/1538-4357/acba8a)
- Ucci, G., Dayal, P., Hutter, A., et al. 2023, *MNRAS*, 518, 3557, doi: [10.1093/mnras/stac2654](https://doi.org/10.1093/mnras/stac2654)
- Williams, H., Kelly, P. L., Chen, W., et al. 2023, *Science*, 380, 416, doi: [10.1126/science.adf5307](https://doi.org/10.1126/science.adf5307)
- Yang, L., Roberts-Borsani, G., Treu, T., et al. 2021, *MNRAS*, 501, 1028, doi: [10.1093/mnras/staa3713](https://doi.org/10.1093/mnras/staa3713)
- Yang, L., Leethochawalit, N., Treu, T., et al. 2022a, *MNRAS*, 514, 1148, doi: [10.1093/mnras/stac1236](https://doi.org/10.1093/mnras/stac1236)
- Yang, L., Morishita, T., Leethochawalit, N., et al. 2022b, *ApJL*, 938, L17, doi: [10.3847/2041-8213/ac8803](https://doi.org/10.3847/2041-8213/ac8803)
- Zitrin, A., Fabris, A., Merten, J., et al. 2015, *ApJ*, 801, 44, doi: [10.1088/0004-637X/801/1/44](https://doi.org/10.1088/0004-637X/801/1/44)